

---

# POViT: Vision Transformer for Multi-objective Design and Characterization of Nanophotonic Devices

---

**Xinyu Chen**<sup>1,†</sup>      **Renjie Li**<sup>1,2,†</sup>      **Yueyao Yu**<sup>1,†</sup>  
 119010032@link.cuhk.edu.cn    renjieli@link.cuhk.edu.cn    yueyaoyu@link.cuhk.edu.cn

**Yuanwen Shen**<sup>2</sup>      **Wenye Li**<sup>\*,3</sup>      **Zhaoyu Zhang**<sup>\*,1,2</sup>  
 ywshen@cuhk.edu.cn      wyli@cuhk.edu.cn      zhangzy@cuhk.edu.cn

**Yin Zhang**<sup>\*,3</sup>  
 yinzhang@cuhk.edu.cn

<sup>1</sup> School of Science and Engineering, The Chinese University of Hong Kong, Shenzhen

<sup>2</sup> Shenzhen Key Laboratory of Semiconductor Lasers

<sup>3</sup> School of Data Science, The Chinese University of Hong Kong, Shenzhen

† indicates equal contribution, \* indicates corresponding authors

## Abstract

We solve a fundamental challenge in semiconductor IC design: the fast and accurate characterization of nanoscale photonic devices. Much like the fusion between AI and EDA, many efforts have been made to apply DNNs such as convolutional neural networks (CNN) to prototype and characterize next-gen optoelectronic devices commonly found in photonic integrated circuits (PICs). These prior works generally strive to predict the quality factor ( $Q$ ) and modal volume ( $V$ ) of for instance, photonic crystals, with ultra-high accuracy and speed. However, state-of-the-art models are still far from being directly applicable in the real-world: e.g. the correlation coefficient of  $V$  ( $V_{coeff}$ ) is only about 80%, which is much lower than what it takes to generate reliable and reproducible nanophotonic designs. Recently, attention-based transformer models have attracted extensive interests and been widely used in CV and NLP. In this work, we propose the first-ever Transformer model (POViT) to efficiently design and simulate semiconductor photonic devices with multiple objectives. Unlike the standard Vision Transformer (ViT), we supplied photonic crystals as data input and changed the activation layer from GELU [1] to an absolute-value function (ABS). Our experiments show that POViT exceeds results reported by previous models significantly. The correlation coefficient  $V_{coeff}$  increases by over 12% (i.e., to 92.0%) and the prediction errors of  $Q$  is reduced by an order of magnitude, among several other key metric improvements. Our work has the potential to drive the expansion of EDA to fully automated photonic design. The complete dataset and code will be released to aid researchers endeavoring in the interdisciplinary field of physics and computer science<sup>1</sup>.

## 1 Introduction

Recently, Deep Learning (DL) have been widely utilized in multiple fields such as medical imaging [2, 3], NLP [4, 5], autonomous driving [6], face recognition [7] and object detection [8]. Neural

<sup>1</sup>Our code are publicly available at: [www.github.com/.../...](http://www.github.com/...)

network can process data effectively and learn rich representations by its strong capacity in dealing with high-dimensional massive data, Impressed by the application prospects of DL, some works have tried Multi-Layer Perceptrons (MLPs) [9–17] and Convolutional Neural Networks (CNNs) [9–13, 18] to design and optimize optoelectronic devices such as nanoscale lasers.

The behavior of nanoscale lasers can be characterized by calculating the material gain in the quantum well/dot and the transverse/longitudinal modes in the defect microcavity [19, 20]. However, the traditional method for designing nanoscale lasers is usually time-costing and inefficient because all the parameters are adjusted manually via simulation tools like COMSOL and Lumerical, whose finite-difference time-domain (FDTD) or finite element analysis (FEA) method is computationally intensive. Moreover, gradient-based optimization methods will often face difficulties in convergence because of the high-dimensional parameter space associated with physical systems and the presence of multiple local minima [16]. Such complicated design depends heavily on computational tractability and designers’ extensive experience [21]. If DL can be successfully applied to this field, there is no doubt that it will save tremendous amount of effort and resources in designing a well-formulated photonic device.

However, it seems that traditional models like CNNs and MLPs are confronted with their performance bottleneck when dealing with physics-related jobs. For example, it is quite hard to increase the correlation coefficient  $V_{coeff}$  by adjusting DNN’s hyperparameters or gradient-based optimization algorithms only. That is why the Vision Transformer, which is a popular topic nowadays based on a unique attention mechanism [4], caught our eyes. Impressed by transformers’ outstanding performance in a variety of engineering tasks, our paper investigates several quintessential models including the original Vision Transformer (ViT) [22], Convolutional Vision Transformer (CvT) [23], and our own version of ViT applied to designing and characterizing Photonic Crystal (PC) nanocavities. PCs are core components of high-performance nanoscale semiconductor lasers used in next-gen photonic integrated circuits (PICs) [20, 24–27]. We thereafter name our final deep learning model *POViT: PhOtonics Vision Transformer*.

## 1.1 Related Works

The InAs/GaAs quantum dot PC nanocavity laser can be experimentally grown on a Silicon wafer substrate [26], but how to predict the quality factor of such a nanophotonic device is still an unsolved problem due to the high complexity of the device’s physical structure. At the same time, it takes much time for the simulation tools to evaluate the prediction performance. Recently, Convolution Neural Network (CNN) [28] has been proposed to train and predict the  $Q$  factor, with a small training dataset (about 1000 samples) and the CNN model did not consider the impact of air hole radius on  $Q$ . The prediction error is about 16%, which is not reliable to be utilized into real practice. Based on works in [28], some works [9] reported that the performance of CNN model could be improved by a larger dataset. Besides  $Q$  factor, another important parameter  $V$  is also an important parameter to evaluate the nano laser’s performance, which is crucial for reducing device footprints and having tight on-chip integration [13]. However, predicting the electric modal volume  $V$  is intractable in [9].

To take the modal volume  $V$  into consideration, [13] succeeded in training  $Q$  and  $V$  simultaneously and maintained tiny test losses, which gets the state-of-the-art result available at present. But the correlation coefficient of  $V$  is relatively low ( $V_{coeff} = 80.5\%$  in the test set). The higher the coefficients  $Q_{coeff}$  and  $V_{coeff}$  are, the more accurate the model’s prediction results will be. Ideally, the best case should be where the coefficients equal 1 for reliable and reproducible design prototypes. Hence, there is still a large gap left for improving  $V_{coeff}$  by adopting better and more advanced DL models.

Transformer models show its power in various tasks, from NLP, CV to basic science areas. The Transformer was first introduced in [4, 29], and developed in computer vision in 2021 [22]. Many works attempted to modify the architecture of ViT [30–32] for better performance or apply Transformer model into multidisciplinary researches [8, 33–40]. For example, a gated axial-attention model [36] was proposed to overcome the problem of lacking data samples in medical image segmentation. It extends the existing transformer architecture by adding control mechanism into the self-attention module. A BERT-based multilingual model in bio-informatics treats DNA sequences as natural sentences and successfully identifies DNA enhancers [39]. Furthermore, a modified transformer network is applied to learn the semantic relationship between objects in collider physics [40].

Different from the original version [22], the Early CNN-embedded Vision Transformer (EarlyVT) replaces the linear layer before the transformer block with a convolutional embedding layer to split the input image into patches [30]. Another model, the Convolutional Vision Transformer (CvT) [23], not only uses the convolutional embedding layer but also substitutes linear projection layers in the Transformer block for deep-wise separable convolution operations.

## 1.2 Contribution

This paper uses the proposed POViT as well as standard CvT and CNN to predict the quality factor  $Q$  and modal volume  $V$  of PC nanocavities. Comparisons are made between the above models, and we found that our POViT successfully beats the state-of-the-art CNN models where the test losses decrease largely (to  $Q_{mse\ loss} = 0.000116$  &  $V_{mse\ loss} = 0.001114$ ) and correlation coefficients improved dramatically (to  $V_{coeff} = 92.0\%$ ) with the minimum prediction error still remaining minuscule ( $Q_{pred\ err} = 0.000035\%$  &  $V_{pred\ err} = 0.000961\%$ ). Our work paves the way for applying Vision Transformer to the rapid multi-objective simulation and optimization of nanophotonic devices without the need for human intervention or trial-and-error iterations. This method bears strong resemblance to the popular marriage of AI and EDA and we mainly aim to empower the rise of fully automated photonic design through our efforts. In this paper, multi-objective means the ability to predict more than one photonic/electromagnetic property, which in our case are  $Q$  and  $V$ .

Furthermore, we also conducted several experiments to prove the robustness of a special kind of activation layer, which is called ABS [41], that outputs the absolute values from the input. We've shown that the ABS layer can significantly improve the performances relative to conventional activation layers like GELU.

Last but not least, we visualize the self-attention mechanism in the transformer blocks through heatmaps. The heatmap in the following section indicates the contribution from different parts of the nanocavity structure to the laser device's overall quality where regions in lighter colors need more attention from the model.

Our dataset and code will be shared as open source in favor of whom endeavors in the relevant fields of physics and materials science.

## 2 Methods

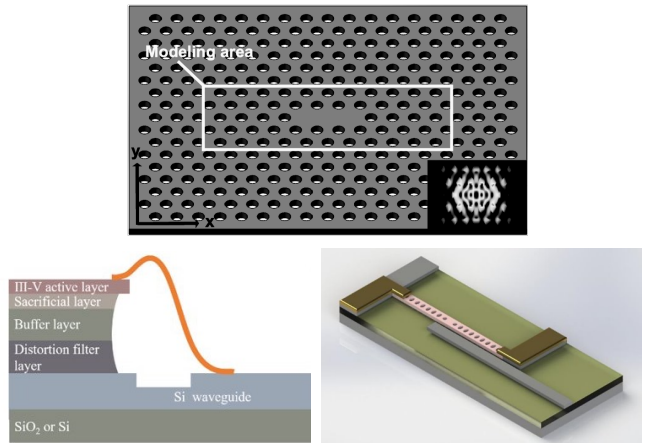


Figure 1: Top: basic structure of the Silicon-based InP PC nanocavity, constituting a typical semiconductor laser. Overall size of the device is around 100 microns in length and 200 nm in thickness. The 54 air holes in the center box will be converted into a 2-D pixel array as the input tensor. Bottom left: side view of the same structure, showing different layers and compositions. Bottom right: a simplified example of a PIC, consisting of nanolasers, PCs and other optical devices.

## 2.1 Physical structure of PC nanocavity laser

Our nanoscale laser is realized by the PC nanocavity shown in Fig.1, which has an regular array of holes in a multi-layer semiconductor (i.e. Si and InP) slab. This particular structure works like a charm because the spontaneous lasing emission is substantially enhanced by the surrounding electromagnetic environment [42], where photons will be gathered to form a laser beam because of the presence of the array of air holes. These holes have a different refractive index compared with the Indium Phosphide (InP) base, which makes photons easily captured and confined. Since the peripheral air holes are far away from the center, they will contribute little to the quality factor  $Q$  and modal volume  $V$ , i.e., these holes do not make a distinct change to the electromagnetic field when they are adjusted. For a glimpse of some of the actual semiconductor nanolasers fabricated by our group, refer to Fig. 7 in the Appendix.

Out of simplicity and resource-friendly purpose, the modeling area only contains 54 holes, which are rounded by the white rectangle (see Fig.1). For holes outside this rectangle, we keep them fixed to dwindle the computational cost. The lattice constant  $a = 320nm$  and the radius of air hole  $r = 89.6nm$  are the standard value, i.e., before changing air holes' positions and radii, the distance between the centers of every pair of adjacent nanocavities is  $320nm$ , and the default radius equals to  $89.6nm$ . The refractive index of InP slab being  $n = 3.4$ , which may differ from other semiconductor materials.

## 2.2 Data collection and pre-processing

The dataset is derived from simulation software FDTD provided by [9] with 12500 samples in all. Each sample contains variations of positions and radii from 54 air holes in the PC structure as the input and the corresponding simulated results  $Q$  and  $V$  as the target. Before forwarding the data samples into the model, we reshape its size into  $N \times 3 \times 5 \times 12$  where "3" represents three channels ( $dx, dy, dr$ ) of the holes and the numbers 5 and 12 denote the height and width of our PC, respectively.

Denote the original position of a hole as  $(x_0, y_0)$  and initial radius as  $r_0$ . We then randomly shift its location horizontally and vertically together with the radius under Gaussian distribution so that its position becomes  $(x', y')$  and radius is  $r'$ . Define  $dx = x' - x_0$ ,  $dy = y' - y_0$ , and  $dr = r' - r_0$ . The Gaussian distribution of  $dx$ ,  $dy$ , and  $dr$  as the input elements follows as:

$$dx \sim \mathcal{N}(\mu = -8.7270 \times 10^{-13}, \sigma^2 = 5 \times 10^{-10}) \quad (1)$$

$$dy \sim \mathcal{N}(\mu = 3.3969 \times 10^{-13}, \sigma^2 = 5 \times 10^{-10}) \quad (2)$$

$$dr \sim \mathcal{N}(\mu = -1.6978 \times 10^{-12}, \sigma^2 = 5 \times 10^{-10}) \quad (3)$$

Due to different numbers of holes in different rows in our PC (shown in Fig. 1), four extraneous zeros are added into the central row, together with two zeros at the top left & bottom right corners, to align the input tensor's column dimension. In practice,  $N = 10000$  so that the remaining 2500 samples can be used as test data. i.e., the size of the training dataset is 10000, and the size of the test dataset is 2500. Furthermore, the 12500 data samples are split randomly so that the features of data samples can be as diverse as possible, by which the generalization capabilities of the designed POViT can be maximized [9, 43]. The sample distribution of the dataset is graphically illustrated in Fig. 8 in the Appendix.

## 2.3 Architecture of POViT & CvT

The self-attention mechanism is a crucial part in the transformer. The input is projected into queries  $\mathbf{Q}$ , keys  $\mathbf{K}$  and values  $\mathbf{V}$  by some linear projections. Transformer will search for the extant key-value pairs and add up these pairs by weights to give out the predictions. The scaled dot-product function of the attention layer is given as:

$$\text{attention}(\mathbf{Q}, \mathbf{K}, \mathbf{V}) = \frac{\mathbf{Q}\mathbf{K}^T}{\sqrt{d}} \mathbf{V} \quad (4)$$

The architecture of POViT is given below (see Fig. 2). Since input size should be divisible by the patch size before patch embedding, which is chosen as 2, the input is added one row of zeros resulting

in the tensor height increasing from 5 to 6. After that, input tensor will be sliced into several patches and processed by patch embedding and positional encoding sequentially to be transferred as token sequences into the transformer encoder.

Meanwhile, this paper compares two different activation functions—ABS and GELU (default)—in Feed Forward Layers (FFN) embedded in the transformer sublayers to examine which one has a better performance. Their expressions are listed below:

$$\text{GELU} = 0.5x(1 + \tanh(\sqrt{\frac{2}{\pi}}(x + 0.044715x^3))) \quad (5)$$

$$\text{ABS} = |x| \quad (6)$$

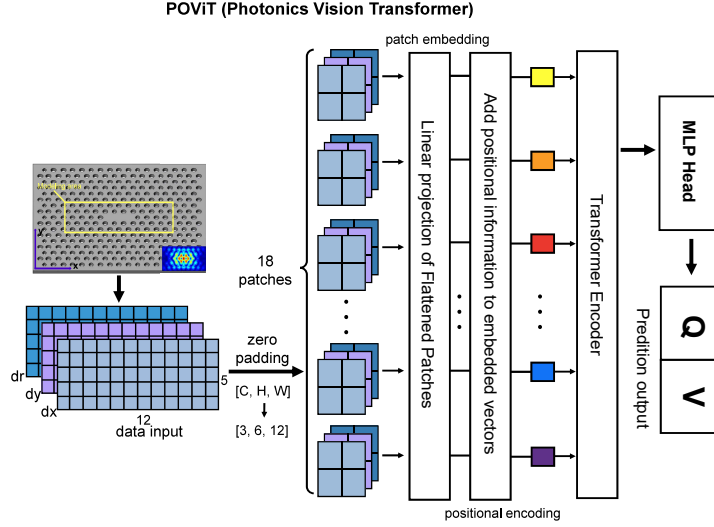


Figure 2: Architecture of the POViT where input tensor shape is  $N \times 3 \times 5 \times 12$  and output tensor shape is  $N \times 2$ . Input is our PC nanolaser converted into images while output is the predicted  $Q$  and  $V$ .

For the architecture of CvT, it bears a resemblance to the ViT except that the usual patch embedding layer that directly slices the image input into several pieces are replaced by a convolutional layer and the linear projections in the transformer block are adjusted to deep-wise separable convolution operations as well.

## 2.4 Data post-processing

To measure the performance of the models, the MSE losses, minimum and converged prediction errors, and correlation coefficients are calculated. The minimum prediction error is measured and recorded by Python at the test stage while the converged one will be averaged at the last few epochs. Consider the targets of the dataset are denoted as  $t_i$  and corresponding prediction outputs are marked as  $p_i$ . The model can be evaluated by:

$$\text{MSE} = \frac{1}{N} \sum_{i=1}^N (t_i - p_i)^2 \quad (7)$$

$$\epsilon_{pred} = \frac{|p_i - t_i|}{t_i} \times 100\% \quad (8)$$

$$\rho(t, p) = \frac{\text{Cov}(t, p)}{\sigma_t \sigma_p} = \frac{E[(t_i - \bar{t})(p_i - \bar{p})]}{\sqrt{\sum_{i=1}^n (t_i - \bar{t})^2} \sqrt{\sum_{i=1}^n (p_i - \bar{p})^2}} \quad (9)$$

The Pearson correlation coefficient  $\rho(t, p) \in [-1, 1]$  can be utilized to measure the linearity between prediction results and targets. If the coefficient is close to 1, then the output will positively corresponds to the target, which means the proposed model perfectly fits in this regression mapping.

### 3 Results & Discussion

#### 3.1 Results

The purpose of proposed POViT is to construct a reliable and efficient method to simulate multi-objective design of nanophotonic devices. Initially, 10000 data samples are chosen and shuffled randomly from the dataset and fed into the model, which runs for 300 epochs each time. After many rounds of experiments, the hyperparameters giving rise to the best performance are listed below. The initial learning rate  $lr = 0.01$ , and the optimizer is *Adam* with the learning rate scheduler as MultiStepLR (milestone=[100, 160, 200] and gamma=0.1). A comprehensive list of hyperparameters we used are reserved in Table 2-3 in the Appendix. Results for the trained POViT using ABS and GELU, respectively, are illustrated in Fig.3-4. The correlation coefficients of training and testing data of  $Q$  happen to be the same. Possible explanations are that since  $Q$  loss is stable at the level of  $10^{-4}$ , such numerical scale has been smaller than the precision of coefficient which has only three significant digits. It also indicates that there is not overfitting during training  $Q$  factor. Since correlation coefficients were not provided in [9, 13], we procured the open-source code from the cited repo and expanded them to include the capability of predicting correlation coefficients. We found that test coefficients in CNNs are calculated to be  $Q_{coeff} = 98.7\%$  and  $V_{coeff} = 80.5\%$ , respectively. From Fig. 4 we can see the best test coefficients in the POViT model are  $Q_{coeff} = 99.4\%$  and  $V_{coeff} = 92.0\%$ , which is 11.5% higher than the best result in previous CNN models.

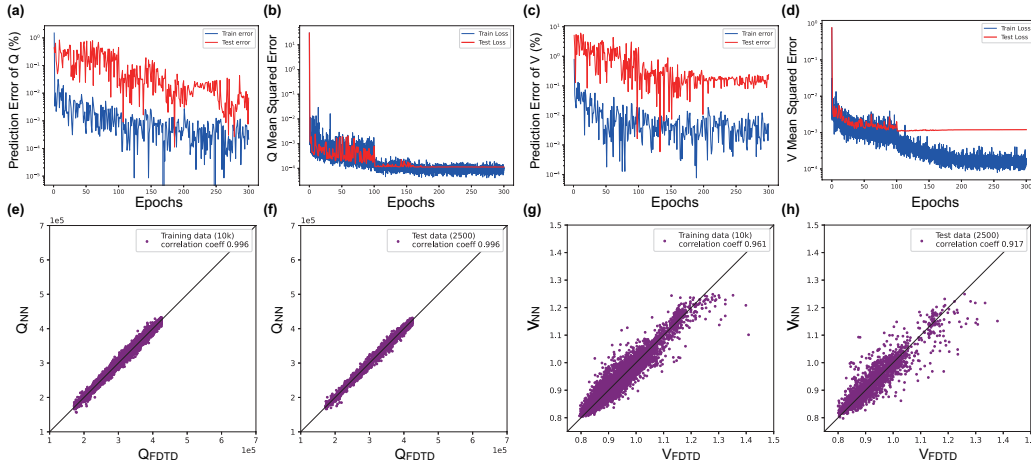


Figure 3: Learning curves and training results for POViT when ABS is used as the activation function. The four plots on the left (a,b,e,f) are for  $Q$ , while the four on the right are for  $V$ .

To compare the performances of different models (CNN, MLP, POViT (ours), CvT), open-source code for CNN are downloaded and augmented from [9] as stated above while results for MLP are followed directly without modifications. Reproduced results for CNN are plotted in Fig. 9-10 and original results for CvT in Fig. 14-15 in the Appendix. Results of POViT and CvT are produced from scratch by us for this work. The dataset is the same with 12500 samples in all during the experiments. Results for  $Q$  and  $V$  across different models are summarized and compared in Table.1. Furthermore, without harming the high test correlation coefficient  $Q_{coeff}$ ,  $V_{coeff}$  also dramatically increases where  $V_{coeff}$  of POViT skyrocketed to 92.0% (see Fig. 4h) and  $V_{coeff}$  of CvT is 88.8%. It indicates the proposed POViT can detect the relationship between L3 PC nanocavities' structure and corresponding optical qualities precisely.

The advantages of the proposed POViT are exuded in the prediction accuracy, convergence speed, and linearity of the model's correlation coefficients (see Fig.3-4). The introduction of self-attention mechanism defeats convolution operation, which used to be the champion in computer vision tasks. Besides, the convergence speed of POViT is fast because the MSE Losses decrease into a low level just in 100 epochs and then maintain itself at a stable state after that. Linearity of POViT, including CvT which combines transformer as well, implies our model's good robustness against noise disturbance.

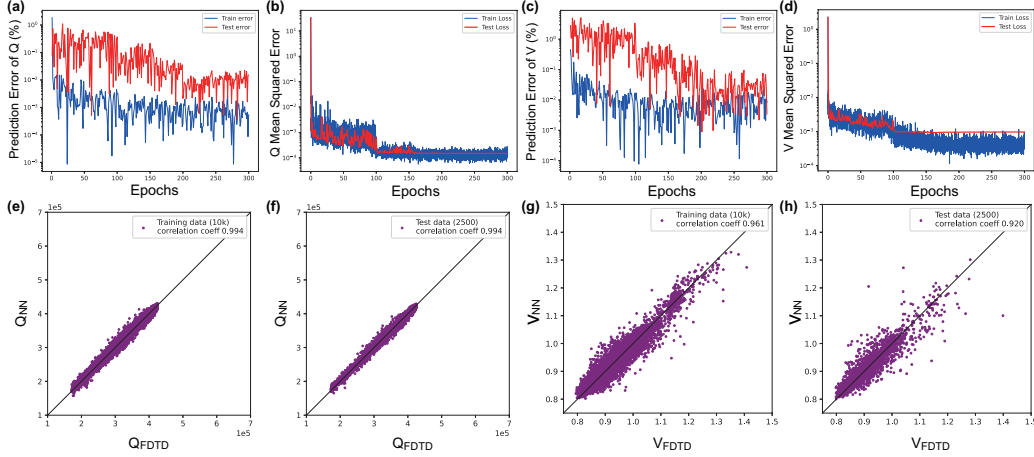


Figure 4: Learning curves and training results for POViT when GELU is used as the activation function. The four plots on the left (a,b,e,f) are for  $Q$ , while the four on the right are for  $V$ .

To make experiments results with POViT more fair and reliable, each time the learning rate was changed, three trials were done and the mean values with uncertainties are summarized (see Table.1). For POViT, the average value of  $Q_{coeff}$  is above 99.0% and  $V_{coeff}$  is around 90.0% with a small deviation, which are notably improved relative to the other models. Furthermore, the improvements in prediction error (both min & conv) of POViT are substantial compared with previous CNN and MLP models where the minimum prediction error has been reduced by an order of magnitude and converged error decreases by over 50%.

Table 1: Comparison of performance metrics for  $Q$  and  $V$  across several models: CNN, MLP, POViT (ours), and CvT. Conv stands for converged. Coeff values are rescaled to percentages. All the data, except for those cited in square brackets, are calculated in the process of producing this work. Except for POViT, which records mean values, data for all the other models are best/optimal values. Raw data used for generating this table are displayed in Fig. 11-13 in the Appendix.

Metrics of $Q$	CNN[9, 13]	CNN <sup>1</sup>	MLP[9]	POViT <sup>2</sup> (ours)	CvT
MSE $Q$	0.000247	0.000160	0.000328	<b>0.000116</b> $\pm$ 0.000009	0.000140
Min pred err $Q$	0.000147%	0.000350%	0.000380%	<b>0.000035</b> $\pm$ 0.000023%	0.000106%
Conv pred err $Q$	0.018953%	0.011352%	0.004676%	<b>0.002953</b> $\pm$ 0.000618%	0.009752%
Coeff $Q$	99.0%	98.7%	98.6%	<b>99.5</b> $\pm$ 0.1%	99.4%
Metrics of $V$					
MSE $V$	0.002520	0.001410	N/A <sup>3</sup>	<b>0.001114</b> $\pm$ 0.000244	0.001458
Min pred err $V$	0.003170%	0.003980%	N/A	<b>0.000961</b> $\pm$ 0.000265%	0.002630%
Conv pred err $V$	0.055800%	0.068351%	N/A	<b>0.036331</b> $\pm$ 0.002708%	0.199203%
Coeff $V$	N/A	80.5%	N/A	<b>90.8</b> $\pm$ 1.8%	88.8%

<sup>1</sup> Reproduced experimental results of CNN using code provided in [9]

<sup>2</sup> Mean results of POViT w/ uncertainties

<sup>3</sup> N/A means no data available.

The relationships between learning rate and MSE loss, correlation coefficient, and prediction error of the proposed POViT embedded with ABS activation are illustrated in Fig.5a-c and comparison between ABS and GELU represented by  $V_{coeff}$  is shown in Fig.5d. For each plot, 8 different learning rates are chosen and experiment for each learning rate is repeated three times to avoid outliers. Mean values from those three runs are calculated and plotted in Fig. 5. In Fig. 5c-d, when the learning rate is around 0.01, the average  $V_{coeff}$  reaches the peak 91.2%. Another sub-peak appears at  $lr = 0.0002$  where average  $V_{coeff} = 90.5\%$ . If the learning rate is larger than 0.01, performance of POViT will plunge greatly so only one more trial was done at  $lr = 0.02$ . We see that in Fig. 5c-d, when  $0.0002 < lr < 0.01$ , there is a valley of  $V_{coeff}$  values which indicates the model has unluckily been trained to reach the local minimum. In consequence, we avoided using those "bad" lr's in our final model. In Fig. 5a, there is a narrow band of lr between 0.0005 and 0.001 where both  $Q$  and  $V$

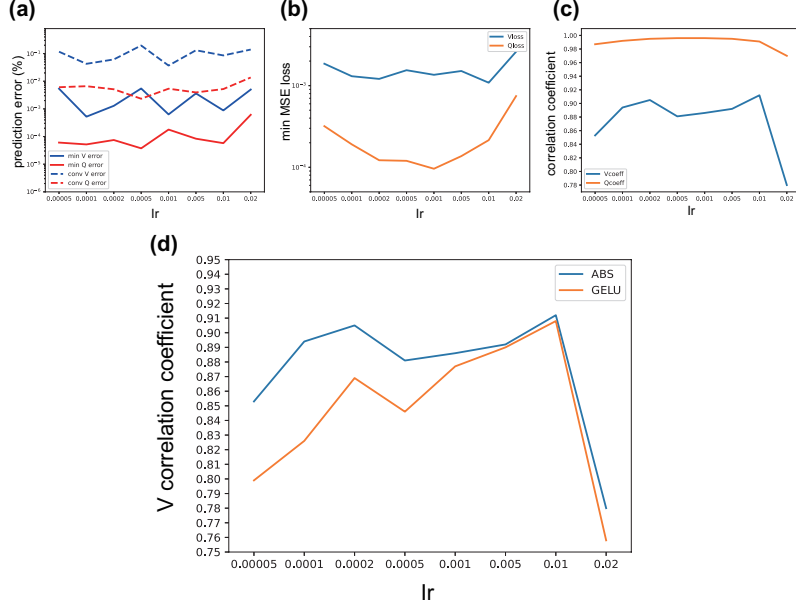


Figure 5: Model performance as a function of learning rates. (a): prediction errors vs.  $lr$ ; (b): minimum MSE loss vs.  $lr$ ; (c): correlation coefficients vs.  $lr$ ; (d):  $V_{coeff}$  calculated with activation functions ABS and GELU vs.  $lr$ , respectively. For each plot, 8  $lr$  values ranging from 0.00005 to 0.02 are chosen. Data points are mean values between 3 separate runs.

reach minimum prediction errors. In Fig. 5b, the average  $V_{loss}$  fluctuates with tiny swings between  $lr = 0.001$  and  $0.002$ , and it reaches a global minimum at  $lr = 0.01$ .

As for the activation layer, which is embedded in the Feed Forward Network (FFN) in the transformer blocks, our experiments found the absolute-value function (ABS) has a recognizably better performance than GELU when  $lr$  is relatively small ( $lr < 0.0005$ ). In Fig. 5d,  $V_{coeff}$  are plotted against  $lr$  to demonstrate a performance contrast in favor of the promising ABS activation layer. When the learning rate gets relatively large ( $lr \approx 0.001$ ), there still exists a small gap where ABS retains an edge over GELU. After  $lr \geq 0.005$  however, the curves of ABS and GELU almost overlap with each other, despite the fact that the curve of the former is always slightly above the latter. Based on the above observation, we conclude that ABS is superior to GELU for our applications.

Lastly, to explore which parts of the PC nanocavity tend to demand more attention from the 6-layer POViT in predicting  $Q$  and  $V$ , we took a look at attention heatmaps. Heatmaps are extracted via a visualizer of POViT during the training and test experiments (see Fig. 6). With depth deepening (i.e. going from top to bottom), there exists more vertical line patterns on the attention maps, which means important information is aggregated to some specific tokens in our data. Within each layer (i.e. in the horizontal direction), where 6 MLP heads are chosen, we can observe some irregularities in the line patterns in those heatmaps. This indicates all the heads work fairly in coordination to produce the final predicted values.

### 3.2 Discussion

It is worthwhile to further study why activation function ABS outperforms GELU when  $lr$  is relatively small. Here, we provide a possible explanation — the dying ReLU phenomenon [44]. Considering the data distribution of  $dx$ ,  $dy$ , and  $dr$  mentioned in section 2.2, input data gather in a small range after normalization and thus a considerable part of data elements are located on the negative half of the axis. As a result, ReLU-like activation functions (e.g. GELU) may suffer from the dying ReLU [44] and some neurons in POViT become inactive with weights reduced close to zero, which will be disadvantageous to the loss result. On the contrary, for ABS, both positive and negative input data elements are retained and treated equally.

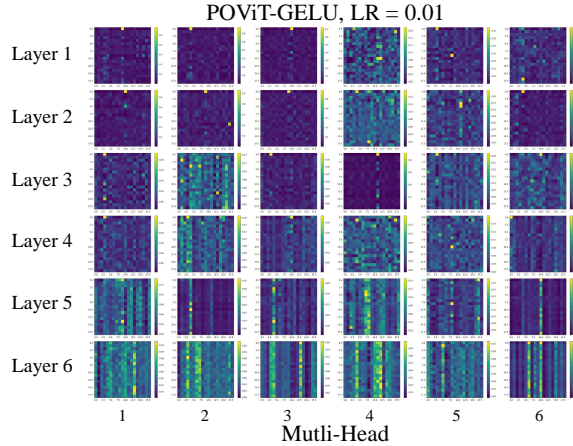


Figure 6: Heatmaps of self-attention in the 6-layer POVit model. Learning rate was taken to be 0.01 and GELU was used as the activation function.

Although the proposed POVit has the edge over other models at its fast and precise multi-objective design and characterization, it still has room for improvement, especially in increasing the correlation coefficient  $V_{coeff}$  and converged prediction error of  $V$ . Future works can be put on fine-tuning the model's hyperparameters like the attention layers' depth or do trials on other optimizers and learning rate schedulers.

## 4 Conclusion

The proposed POVit is the first to introduce Vision Transformer into designing and characterizing nanophotonic devices. Based on self-attention mechanism, POVit successfully predicts multiple objectives such as  $Q$  factor and modal volume  $V$  simultaneously with both high accuracy and reliability when given physical parameters of PC nanocavities. It makes rapid and efficient designs in related engineering and applied sciences fields possible and may become a powerful disruptive alternative to existing simulation tools like FDTD and FEA. The heatmap from transformer blocks also gives some hints for researchers about which parts in their design blueprint will be more important. Our dataset together with code will be released to the community, expecting that it will make a difference in the near future. For this project, we used Pytorch to train the neural networks in the conda environment (anaconda3 2021.11 + Python 3.10.1), where the workstation is equipped with an Intel i7-11800H CPU, an Nvidia GeForce RTX3070 GPU and 16G memory. The average time to run one experiment is about 18 to 20 minutes.

As for limitations of this work, although the best correlation coefficient  $V_{coeff}$  is above 90%, chances are that the numbers would be higher if the POVit model was further fine-tuned. For example, hyperparameters including the learning rate, the depth of the transformer encoder, and dimensions of heads in the attention layer can be adjusted for better performance if possible. More importantly, DL models are data-hungry: more data samples with various features will improve prediction accuracies. However, the data this work used are relatively limited to certain ranges: e.g., simulated  $Q$  factors are below  $5 \times 10^5$  and modal volumes  $V > 0.8$ . If more data with larger  $Q$  and smaller  $V$  are added into the dataset, POVit will be more robust and generalizable. In the future work, we will enlarge our dataset and conduct more trials with different hyperparameters and algorithms. We hope  $V_{coeff}$  can reach above 95% so that POVit can become a reliable and trustworthy simulation tool for researchers in PICs and save them more time than using conventional modeling means. Furthermore, modifications on the proposed POVit model are also expected for improvement by us in the following stage. Lastly, deep reinforcement learning and transfer learning are currently being explored by us to enable fully autonomous EDA-like optimizing tools for nanolasers and PICs.

## Acknowledgement

This work is supported by National Natural Science Foundation of China under Grant No.62174144; Shenzhen Fundamental Research Fund under Grant No.JCYJ20210324115605016 and No.JCYJ20210324120204011; Shenzhen Key Laboratory Project under Grant No.ZDSYS201603311644527; Longgang Key Laboratory Project under Grant No.ZSYS2017003 and No.LGKCZSYS2018000015; Longgang Matching Support Fund No.CXPTPT-2017-YJ-002 and No.201617486; President's Fund (PF01000154); and the Optical Communication Core Chip Research Platform. The authors would like to thank the engineers at the Core Research Facilities (CRF) of SUSTech for their technical support. The authors would like to thank staff members at ITSO of CUHSZ for their persistent support for our computing needs.

The authors declare no conflict of interests.

## References

- [1] Dan Hendrycks and Kevin Gimpel. "Gaussian error linear units (gelus)". In: *arXiv preprint arXiv:1606.08415* (2016).
- [2] June-Goo Lee et al. "Deep learning in medical imaging: general overview". In: *Korean journal of radiology* 18.4 (2017), pp. 570–584.
- [3] Hayit Greenspan, Bram Van Ginneken, and Ronald M Summers. "Guest editorial deep learning in medical imaging: Overview and future promise of an exciting new technique". In: *IEEE transactions on medical imaging* 35.5 (2016), pp. 1153–1159.
- [4] Ashish Vaswani et al. "Attention is all you need". In: *Advances in neural information processing systems* 30 (2017).
- [5] Thomas Wolf et al. "Huggingface's transformers: State-of-the-art natural language processing". In: *arXiv preprint arXiv:1910.03771* (2019).
- [6] Khan Muhammad et al. "Deep learning for safe autonomous driving: Current challenges and future directions". In: *IEEE Transactions on Intelligent Transportation Systems* 22.7 (2020), pp. 4316–4336.
- [7] Guosheng Hu et al. "When face recognition meets with deep learning: an evaluation of convolutional neural networks for face recognition". In: *Proceedings of the IEEE international conference on computer vision workshops*. 2015, pp. 142–150.
- [8] Nicolas Carion et al. "End-to-end object detection with transformers". In: *European conference on computer vision*. Springer, 2020, pp. 213–229.
- [9] Renjie Li et al. "Deep learning-based modeling of photonic crystal nanocavities". In: *Optical Materials Express* 11.7 (2021), pp. 2122–2133.
- [10] Jiaqi Jiang, Mingkun Chen, and Jonathan A Fan. "Deep neural networks for the evaluation and design of photonic devices". In: *Nature Reviews Materials* 6.8 (2021), pp. 679–700.
- [11] Takashi Asano and Susumu Noda. "Iterative optimization of photonic crystal nanocavity designs by using deep neural networks". In: *Nanophotonics* 8.12 (2019), pp. 2243–2256.
- [12] Robin Singh, Anu Agarwal, and Brian W Anthony. "Mapping the design space of photonic topological states via deep learning". In: *Optics Express* 28.19 (2020), pp. 27893–27902.
- [13] Renjie Li et al. "Smart and Rapid Design of Nanophotonic Structures by an Adaptive and Regularized Deep Neural Network". In: *Nanomaterials* 12.8 (2022), p. 1372.
- [14] Wei Ma et al. "Deep learning for the design of photonic structures". In: *Nature Photonics* 15.2 (2021), pp. 77–90.
- [15] Peter R Wiecha et al. "Deep learning in nano-photonics: inverse design and beyond". In: *Photonics Research* 9.5 (2021), B182–B200.
- [16] Yangming Ren et al. "Genetic-algorithm-based deep neural networks for highly efficient photonic device design". In: *Photonics Research* 9.6 (2021), B247–B252.
- [17] Zihao Ma and Yu Li. "Parameter extraction and inverse design of semiconductor lasers based on the deep learning and particle swarm optimization method". In: *Optics Express* 28.15 (2020), pp. 21971–21981.
- [18] Alec M Hammond and Ryan M Camacho. "Designing integrated photonic devices using artificial neural networks". In: *Optics express* 27.21 (2019), pp. 29620–29638.

- [19] Xun Li. *Optoelectronic devices: design, modeling, and simulation*. Cambridge University Press, 2009.
- [20] Simon M Sze, Yiming Li, and Kwok K Ng. *Physics of semiconductor devices*. John Wiley & sons, 2021.
- [21] Wim Bogaerts and Lukas Chrostowski. “Silicon photonics circuit design: methods, tools and challenges”. In: *Laser & Photonics Reviews* 12.4 (2018), p. 1700237.
- [22] Alexey Dosovitskiy et al. “An image is worth 16x16 words: Transformers for image recognition at scale”. In: *arXiv preprint arXiv:2010.11929* (2020).
- [23] Haiping Wu et al. “Cvt: Introducing convolutions to vision transformers”. In: *Proceedings of the IEEE/CVF International Conference on Computer Vision*. 2021, pp. 22–31.
- [24] Tin Komljenovic et al. “Heterogeneous silicon photonic integrated circuits”. In: *Journal of Lightwave Technology* 34.1 (2016), pp. 20–35.
- [25] Mark A Foster et al. “Broad-band optical parametric gain on a silicon photonic chip”. In: *Nature* 441.7096 (2006), pp. 960–963.
- [26] Taojie Zhou et al. “Continuous-wave quantum dot photonic crystal lasers grown on on-axis Si (001)”. In: *Nature communications* 11.1 (2020), pp. 1–7.
- [27] Yoshihiro Akahane et al. “High-Q photonic nanocavity in a two-dimensional photonic crystal”. In: *nature* 425.6961 (2003), pp. 944–947.
- [28] Takashi Asano and Susumu Noda. “Optimization of photonic crystal nanocavities based on deep learning”. In: *Optics express* 26.25 (2018), pp. 32704–32717.
- [29] Colin Raffel et al. “Exploring the limits of transfer learning with a unified text-to-text transformer”. In: *arXiv preprint arXiv:1910.10683* (2019).
- [30] Tete Xiao et al. “Early convolutions help transformers see better”. In: *Advances in Neural Information Processing Systems* 34 (2021), pp. 30392–30400.
- [31] Ilya O Tolstikhin et al. “Mlp-mixer: An all-mlp architecture for vision”. In: *Advances in Neural Information Processing Systems* 34 (2021).
- [32] Ze Liu et al. “Swin transformer: Hierarchical vision transformer using shifted windows”. In: *Proceedings of the IEEE/CVF International Conference on Computer Vision*. 2021, pp. 10012–10022.
- [33] Aditya Prakash, Kashyap Chitta, and Andreas Geiger. “Multi-modal fusion transformer for end-to-end autonomous driving”. In: *Proceedings of the IEEE/CVF Conference on Computer Vision and Pattern Recognition*. 2021, pp. 7077–7087.
- [34] Cunjun Yu et al. “Spatio-temporal graph transformer networks for pedestrian trajectory prediction”. In: *European Conference on Computer Vision*. Springer. 2020, pp. 507–523.
- [35] Yilun Chen et al. “Attention-based hierarchical deep reinforcement learning for lane change behaviors in autonomous driving”. In: *Proceedings of the IEEE/CVF Conference on Computer Vision and Pattern Recognition Workshops*. 2019.
- [36] Jeya Maria Jose Valanarasu et al. “Medical transformer: Gated axial-attention for medical image segmentation”. In: *International Conference on Medical Image Computing and Computer-Assisted Intervention*. Springer. 2021, pp. 36–46.
- [37] Zhihong Chen et al. “Generating radiology reports via memory-driven transformer”. In: *arXiv preprint arXiv:2010.16056* (2020).
- [38] Kevin Chen et al. “Topological planning with transformers for vision-and-language navigation”. In: *Proceedings of the IEEE/CVF Conference on Computer Vision and Pattern Recognition*. 2021, pp. 11276–11286.
- [39] Nguyen Quoc Khanh Le et al. “A transformer architecture based on BERT and 2D convolutional neural network to identify DNA enhancers from sequence information”. In: *Briefings in bioinformatics* 22.5 (2021), bbab005.
- [40] Vinicius Mikuni and Florencia Canelli. “Point cloud transformers applied to collider physics”. In: *Machine Learning: Science and Technology* 2.3 (2021), p. 035027.
- [41] Yueyao Yu and Yin Zhang. “Householder-Absolute Neural Layers For High Variability and Deep Trainability”. In: *arXiv preprint arXiv:2106.04088* (2021).
- [42] Hatice Altug, Dirk Englund, and Jelena Vučković. “Ultrafast photonic crystal nanocavity laser”. In: *Nature physics* 2.7 (2006), pp. 484–488.
- [43] Ian Goodfellow, Yoshua Bengio, and Aaron Courville. *Deep learning*. MIT press, 2016.

[44] Lu Lu. “Dying ReLU and Initialization: Theory and Numerical Examples”. In: *Communications in Computational Physics* 28.5 (2020), pp. 1671–1706.

## A Appendix

Table 2: Additional Hyper-parameters of POViT

Hyper-parameter	Value
input img size	$[B, C, H, W]=[N, 3, 6, 12]$
patch size	$[B, C, H, W]=[N, 3, 2, 2]$
num of patches	$(6 \times 12) \div (2 \times 2) = 18$
patch dim	$3 \times 2 \times 2 = 12$
embedded patch dim	36
Transformer dim	$36 \times 18 = 648$
Transformer depth	6
Transformer num of heads	6
Transformer dim per head	12
Transformer mlp dim	72
pooling method	cls
output size	$[B, O]=[N, 2]$

Table 3: Additional Hyper-parameters of CvT

Hyper-parameter	Value
input channels	3, 12, 24
input img size	$5 \times 12, 3 \times 6, 2 \times 3$
output channels	12, 24, 36
output img size	$3 \times 6, 2 \times 3, 1 \times 2$
patch size	$3 \times 3, 3 \times 3, 2 \times 2$
patch stride	2, 2, 1
patch padding	1, 1, 0
attention depth	3, 2, 1
num of heads	4, 8, 12
mlp ratio	2, 2, 2
dim of mlp head	$36 \times 1 \times 2 = 72$

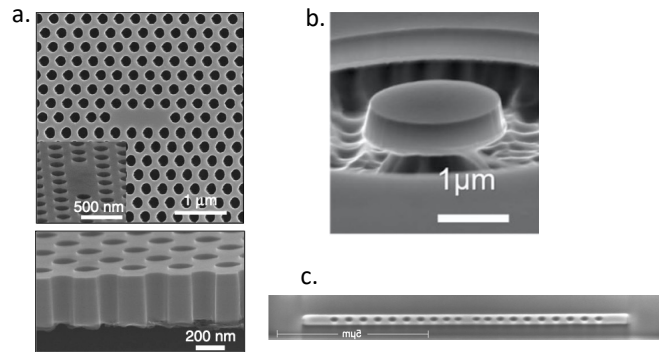


Figure 7: Examples of fabricated nanoscale semiconductor lasers by our group. a: L3 PC nanocavity laser. b: GaAs quantum dot microdisk laser. c: PC nanobeam laser.

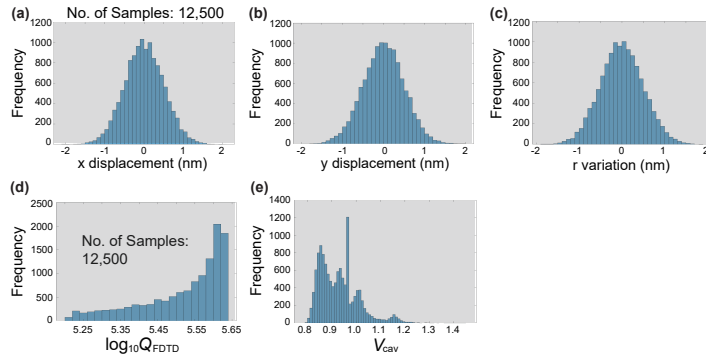


Figure 8: Dataset used for training POViT. Top row: input data. Bottom row: output targets.

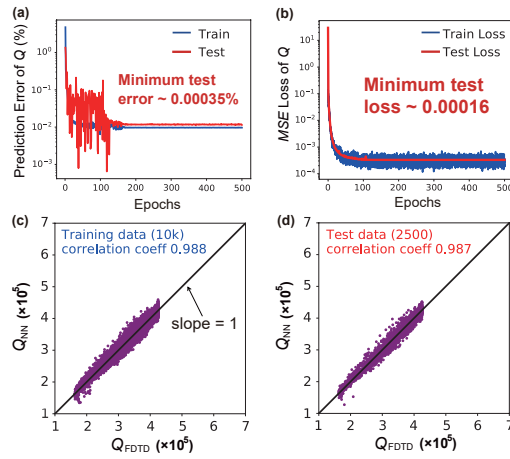


Figure 9: Learning curves and training results of the reproduced (i.e. augmented) CNN model for predicting Q used in this work.

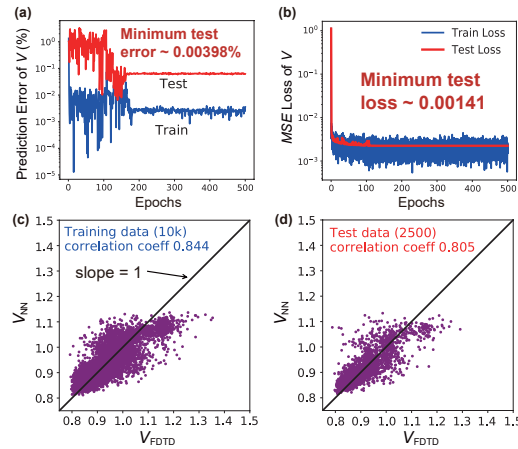


Figure 10: Learning curves and training results of the reproduced (i.e. augmented) CNN model for predicting V used in this work.

Lr = 0.00005	ABS1	Qmin	0.00000	Vmin	0.000180
		Qconv	0.00654	Vconv	0.049234
		Qloss	0.000285	Vloss	0.001642
		Q	0.988	V	0.8720
	ABS2	Qmin	0.000147	Vmin	0.01565
		Qconv	0.001328	Vconv	0.24861
		Qloss	0.000282	Vloss	0.002262
		Q	0.9880	V	0.8200
	ABS3	Qmin	0.0000346	Vmin	0.0002702
		Qconv	0.01036	Vconv	0.052529
		Qloss	0.000389	Vloss	0.0001663
		Q	0.9840	V	0.868
Avg	Qmin	0.0000606	Vmin	0.005367	
	Qconv	0.006076	Vconv	0.11167	
	Qloss	0.000319	Vloss	0.001856	
	Q	0.987	V	0.853	
Lr = 0.0001	ABS1	Qmin	0.00000	Vmin	0.001331
		Qconv	0.001549	Vconv	0.08713
		Qloss	0.000198	Vloss	0.001308
		Q	0.992	V	0.889
	ABS2	Qmin	0.00004326	Vmin	0.0002315
		Qconv	0.009837	Vconv	0.02858
		Qloss	0.000192	Vloss	0.001362
		Q	0.992	V	0.891
	ABS3	Qmin	0.0001125	Vmin	0.00001
		Qconv	0.008457	Vconv	0.01229
		Qloss	0.000184	Vloss	0.001246
		Q	0.993	V	0.903
Avg	Qmin	0.00005193	Vmin	0.0005231	
	Qconv	0.006615	Vconv	0.04267	
	Qloss	0.000191	Vloss	0.001305	
	Q	0.992	V	0.894	
Lr = 0.001	ABS1	Qmin	0.00003459	Vmin	0.001471
		Qconv	0.003462	Vconv	0.07320
		Qloss	0.000093	Vloss	0.001260
		Q	0.996	V	0.896
	ABS2	Qmin	0.0000	Vmin	0.00004528
		Qconv	0.006052	Vconv	0.01738
		Qloss	0.000088	Vloss	0.001199
		Q	0.996	V	0.890
	ABS3	Qmin	0.00050191	Vmin	0.0003795
		Qconv	0.006604	Vconv	0.01999
		Qloss	0.000106	Vloss	0.001615
		Q	0.996	V	0.872
Avg	Qmin	0.0001788	Vmin	0.00063197	
	Qconv	0.005373	Vconv	0.03686	
	Qloss	0.000096	Vloss	0.001358	

Figure 11: Excerpt of raw data used for generating Table 1 and 2.

Lr = 0.01	ABS1	Q	0.996	V	0.886
		Qmin	0.00005189	Vmin	0.001437
		Qconv	0.003811	Vconv	0.06989
		Qloss	0.000333	Vloss	0.001017
	ABS2	Q	0.986	V	0.913
		Qmin	0.0001125	Vmin	0.0005903
		Qconv	0.005988	Vconv	0.1544
		Qloss	0.000112	Vloss	0.001096
	ABS3	Q	0.996	V	0.917
		Qmin	0.00009	Vmin	0.0006123
		Qconv	0.005850	Vconv	0.03276
		Qloss	0.000201	Vloss	0.001147
Avg	Q	0.992	V	0.907	
	Qmin	0.00005767	Vmin	0.0008799	
	Qconv	0.005217	Vconv	0.08568	
	Qloss	0.000215	Vloss	0.001087	
	Q	0.991	V	0.912	

GELU Vcoeff data				
Lr = 0.00005	0.802	0.798	0.796	0.799
Lr = 0.0001	0.819	0.838	0.822	0.826
Lr = 0.0002	0.859	0.869	0.878	0.869
Lr = 0.0005	0.831	0.851	0.855	0.846
Lr = 0.001	0.891	0.869	0.871	0.877
Lr = 0.005	0.889	0.895	0.886	0.890
Lr = 0.01	0.888	0.920	0.917	0.908
Lr = 0.02	0.748	0.763	0.763	0.758
GeLu Qcoeff data				
Lr = 0.01	0.991	0.994	0.994	0.993

GELU Q loss				
0.000227	0.000148	0.000150	→	0.000175
V loss				
0.00139	0.000925	0.001028	→	0.001114
Q min err				
0.0001557	0.0003631	0.0002078	→	0.000242
V min err				
0.000741	0.000887	0.001255	→	0.000961
Q conv err				
0.0.01849	0.01207	0.004292	→	0.01161
V conv err				
0.0.03706	0.03860	0.03333	→	0.03633

Figure 12: Fig. 11 continued.

GELU		
0.000122	Min 0.00001731	Coeff 0.995
	Conv 0.0026126	
0.000120	Min 0.00006065	Coeff .995
	Conv 0.0025802	
0.000106	Min 0.00002595	Coeff 0.996
	Conv 0.003666	
Loss	0.000116	
Min	0.000350	
Conv	0.002953	
Coeff	.995	

Figure 13: Fig. 11 continued.

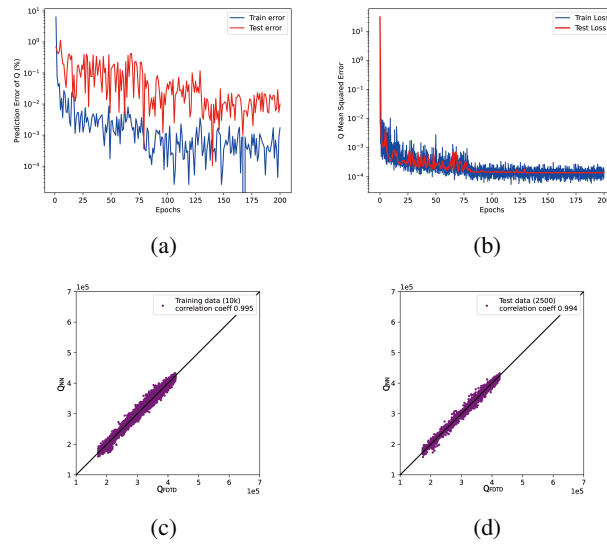


Figure 14: Learning curves and training results of the CvT model for predicting Q used in this work

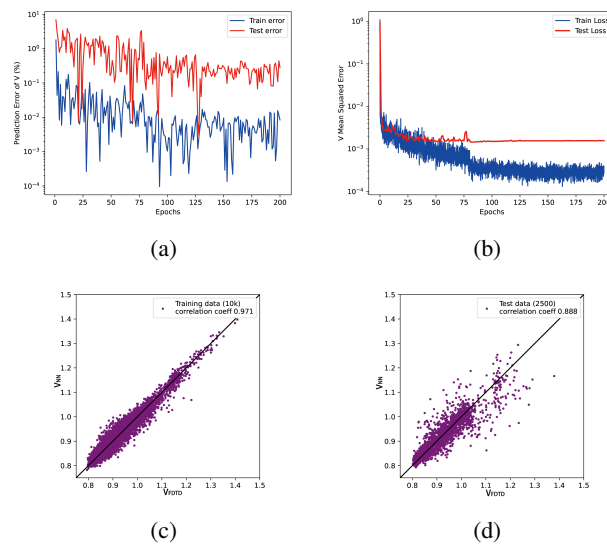


Figure 15: Learning curves and training results of the CvT model for predicting V used in this work